3D c-AFM IMAGING OF CONDUCTIVE FILAMENTS IN HfO_2 RESISTIVE SWITCHING DEVICES

An Undergraduate Research Scholars Thesis

by

SARAH HAMMOCK

Submitted to the Undergraduate Research Scholars program at
Texas A&M University
in partial fulfillment of the requirements for the designation as an

UNDERGRADUATE RESEARCH SCHOLAR

Approved by Research Advisor: Dr. Patrick Shamberger

May 2017

Major: Chemical Engineering

TABLE OF CONTENTS

ABSTRACT

3D c-AFM Imaging of Conductive Filaments in HfO_2 Resistive Switching Devices

Sarah Hammock
Department of Chemical Engineering
Texas A&M University

Research Advisor: Dr. Patrick Shamberger
Department of Materials Science
Texas A&M University

Resistive switching in metal-insulator-metal devices is promising as an alternative to flash memory. The change in resistance from insulating to conducting and back again is theoretically caused by the formation and partial destruction of conductive filaments composed of a metal or oxide structure. These filaments have a significant effect on device performance and stability. However, due to their small size (nm range) and location within the device, the filaments are difficult to study directly. Various techniques such as TEM, SEM, and c-AFM have been used to obtain 2D or 3D images of the filaments in an attempt to determine their morphology, conductivity, and composition. In this study, AFM and c-AFM were used to investigate the topography and local conductivity of the oxide layer and construct a 3D image of a conductive filament in formed p+Si|HfO_2|Cu devices. Damage to the oxide layer was found to vary with both oxide crystallinity and forming voltage, conductive regions were found to be associated with the damaged areas, and the 3D data collected for the filament revealed an hourglass morphology.

ACKNOWLEDGEMENTS

First, a thank you to Dr. Shamberger for his guidance and assistance through all aspects of this project. Much thanks to Heidi Clarke, who performed device fabrication and a portion of the AFM results, as well as preparing figures and guiding me in data collection and analysis. Thank you to Laura Deremo and Joseph Anderson for their work on device formation.

NOMENCLATURE

RRAM	Resistive Random Access Memory
LRS	Low Resistance State
HRS	High Resistance State
ON state	Conductive (low resistance) state
OFF state	Non-conductive (high resistance) state
BE	Bottom electrode
TE	Top Electrode
c-AFM	Conductive Atomic Force Microscopy
TEM	Transmission Electron Microscopy
STEM	Scanning Tunneling Electron Microscopy
SEM	Scanning Electron Microscopy

CHAPTER I

INTRODUCTION

Resistive switching is a phenomenon in which an insulator, which is initially in a high resistance state, can be switched between conductive and insulating states under application of voltage bias. The effect generally occurs when a voltage is applied to a transition metal oxide (such as HfO_2) sandwiched between top and bottom conductive contacts (such as copper and p-doped silicon), driving ion migration to form a filament. Since ion migration under voltage application is non-linear, the resistance state of the device does not change in the absence of an applied bias, creating a non-volatile type of memory storage. One of the obstacles to implementing resistive switching devices is the large variability in their on- and off-state resistances. When a device is created, it is initially in the off state, or non-conductive state. The process of switching the device to a conductive state for the first time is known as forming. When a device is formed, a conductive filament of metal ions or oxygen vacancies grows through the semiconductor layer to connect the two metal layers. The filament growth depends on many factors, such as the oxide and metal layers used, the structure of the oxide, and the maximum current allowed to flow through the filament. It would be useful to know the shape and size of the filament, as these parameters may affect the resistance of the device in the on-state, as well as provide insight into how the filaments form. However, due to the nanoscale size of the filament and its location in the interior of the device, obtaining direct observations of the conductive filament is difficult. The techniques that have been used thus far include transmission electron microscopy (TEM) and surface and scalpel conductive atomic force microscopy (c-AFM).

Transmission Electron Microscopy

Transmission Electron Microscopy (TEM) is a technique in which a beam of electrons passes through a sample, resulting in an image or a diffraction pattern which is recorded and used to determine the structure of the sample. TEM has been used to image conductive filaments in several device structures[1-7]. Kim reports the observation of filaments of non-stoichiometric oxide in Pt|TiO_2|Pt devices using TEM[1]. Several filaments appeared to connect the two Pt electrodes when the device was in the ON state, while there were only incomplete filaments found in devices in the OFF state. This supports the theory that the resistive switching phenomenon is due to the formation of conductive filaments between the top and bottom electrodes. Similar results were shown for a W|GeTe|Cu structure, but the filaments were composed of Cu [2]. Overall, filament composition appears to depend on various factors such as the electrode composition, the oxide composition, and the polarity of the forming voltage.

In addition to standard TEM, a related technique called Scanning Transmission Electron Microscopy with Electron Energy Loss Spectroscopy (STEM-EELS) has been used to study the filaments in resistive switching devices. In STEM-EELS, an electron beam passes through the sample and is routed through a magnetic prism. This prism deflects the electrons according to their energy, allowing the identification of the chemical nature of the atoms in the sample. In their study on conductive filaments in TiN|HfO_2|c-AFM tip devices (in which the top electrode was replaced with a c-AFM tip), Calka et al. used STEM-EELS to obtain cross-sectional images of the filament as well as composition information [8]. This required locating the conduction region using scanning spreading resistance microscopy (SSRM) and then cutting through the region using a focused ion beam. The resulting images showed an oxygen deficiency in the

conductive region, implying that in this case, the filament may have been composed of oxygen vacancies [8].

There are significant downsides to TEM. First, TEM does not provide any direct information on the conductivity of the filaments and surrounding oxide. In addition, since it is a 2D technique, it provides limited information on the morphology of the sample. It is also difficult to locate the filament using TEM if the device area is large, as TEM cannot identify changes to the device that could signify the location of a filament. As for STEM-EELS, obtaining a cross-section of the device is necessary, but using a focused ion beam can damage the sample and obscure the results.

Conductive Atomic Force Microscopy

Conductive Atomic Force Microscopy, or c-AFM, is another technique that has been used to study the conductive filaments in resistive switching devices. AFM provides measurements of surface topography by moving a sharp tip across the material. The tip is attached to a cantilever, where a laser beam is focused. As the tip moves over hills and valleys on the surface, the cantilever moves and the laser is deflected. The deflection of the laser is used to map the topography of the surface. c-AFM does the same thing, except that the tip is composed of a conductive material, allowing current data to be taken at the same time as the topography data. This is useful for determining the location of conductive filaments in the device. Brivio et al. used this technique to study TiN|HfO_2|c-AFM tip devices [9]. Conductive and topographic maps were created of not only the unformed devices, but of formed and reset devices as well. This enabled Brivio et al. to correlate the locations of filaments with areas of untouched devices that were slightly conductive to begin with [9]. c-AFM also allowed them to

speculate about the morphology and the method of formation of the filaments, but it provided no direct information on their morphology or chemical structure. Deleruyelle et al. performed a similar study on Ti|NiO|c-AFM tip devices [10]. They found the same trend of filaments forming at areas that were initially weakly conductive. Iglesias et al. found that conductive paths in HfO_2 are linked to grain boundaries [11] and Lanza et al. found that filaments in HfO_2 tend to form along grain boundaries [12]. c-AFM measurements also enabled them to confirm the retention of the filaments after a significant amount of time; again, however, c-AFM could not provide any direct information on anything beyond the device surface [10]. Despite these limitations, a variation on this surface c-AFM technique was utilized in this study, in which a device was formed and then a wet etchant was used to remove the top copper contact before c-AFM measurements were obtained.

Surface c-AFM yields useful information about resistive switching filaments; however, it provides only a 2D image. A slice-and-view technique has recently been developed that allows the creation of 3D models of filaments. First, a surface c-AFM scan is performed. Next, an AFM tip is used to scratch away a layer of the device. The c-AFM tip is then used to take another surface reading, and the process is repeated until the bottom electrode is reached. The series of 2D images is used to construct a 3D model of the filament. Two studies which made some of the first uses of this technique were performed for cells of $TiN|Al_2O_3|Cu$ [13, 14]. Another study was performed on $Cu|Al_2O_3|$tip devices, meaning that the c-AFM tip itself was used as the top electrode [15]. While this made it easier to locate the conductive filaments, the small size of the top electrode likely affected filament formation. So far HfO_2 devices have not been analyzed with the slice-and-view technique.

CHAPTER II

METHODS

Device fabrication

Devices consisted of a heavily p-doped silicon substrate bottom electrode, a hafnium oxide dielectric layer, and a Cu top electrode. <100> Si substrates, heavily doped with boron to form p+ doped Si, were obtained from a commercial distributor. Buffered oxide etch was used to rinse the wafers and remove native oxides from the surface. Afterward, the wafers were loaded into an ALD chamber (high vacuum Atomic Layer Deposition Cambridge Nanotech Fiji chamber) on thermal mode in order to fabricate the HfO_2 layer. An O_2 plasma was used as the oxidizer, while Tetrakis(dimethylamido)hafnium (TDMA-Hf) held at 75 ^oC was used as the Hf source, and N_2 was used as the carrier/purge gas. Different deposition and post-deposition annealing temperatures were used to obtain different oxide microstructures. These temperatures are shown in Table 1 below. Regardless of the deposition and annealing conditions, 30 nm of HfO_2 was deposited on each wafer, and the wafers were broken into smaller squares.

Table 1: Deposition and forming conditions for the HfO_2 layer, and the resulting HfO_2 crystallinity.

Sample Name	Growth Temp °C	Annealing Temp °C	Crystallinity
SA	100	400	Amorphous (AFM incomplete)
SB	100	600	Polycrystalline (more randomly oriented)
SC	250	---	Polycrystalline (less randomly oriented)

The top electrode, copper, was patterned as a 20 x 20 µm square connected by a thin 5 µm wide neck to a larger 400 x 400 µm probe pad used for contacting the device with a W probe tip during electrical testing (r = 1 µm). The process for deposition of the top contacts is shown in Figure 1.

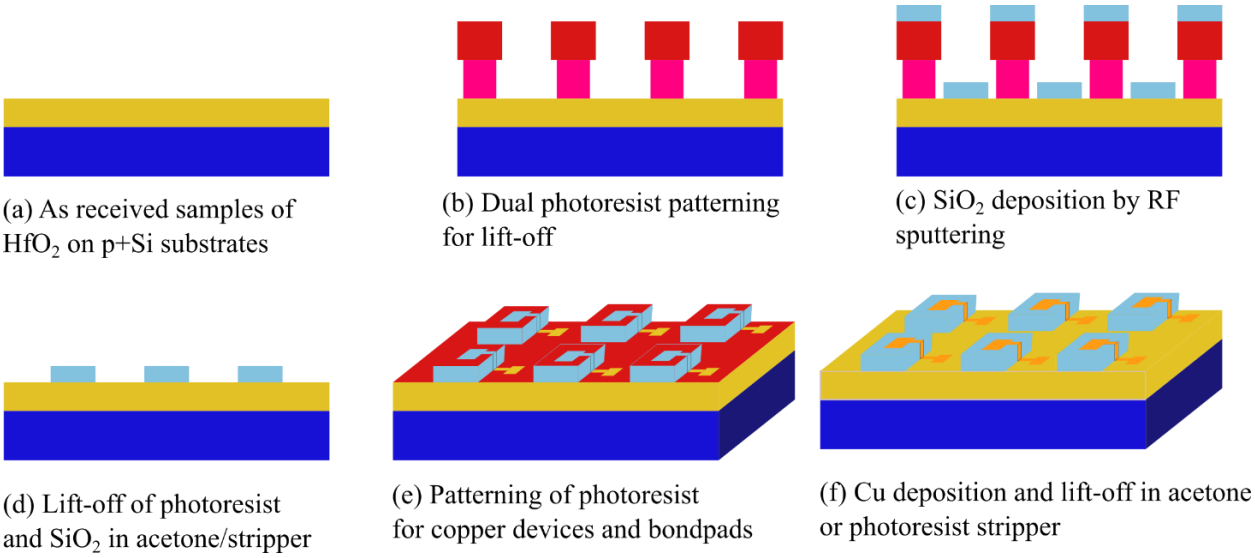

Figure 1: Process flow for deposition of copper top electrodes for several devices.

Isolation layers consisted of 70 nm of SiO_2 and 10 nm of Cr to prevent the formation of a filament beneath the bond pad, while maintaining an electrical connection between the bond-pad and device-pad across the step edge. The devices and bond pads were organized in squares, with 184 devices per square. This pattern was defined using lift-off photolithography. Successive SiO_2, Cr, and Cu films were deposited on top of dual positive photoresist layers (LOR 3A and AZ5214), which were removed in acetone and AZ400T photoresist stripper. SiO_2 was deposited by RF sputtering from a SiO_2 target in 4% O_2/96% Ar gas atmosphere at 3.0E-3 Torr. Cr (10 nm) and Cu (25 nm) films were deposited via e-beam evaporation with a base pressure of at least 5.0E-6 Torr. The resulting devices and their layout are shown in Figure 2.

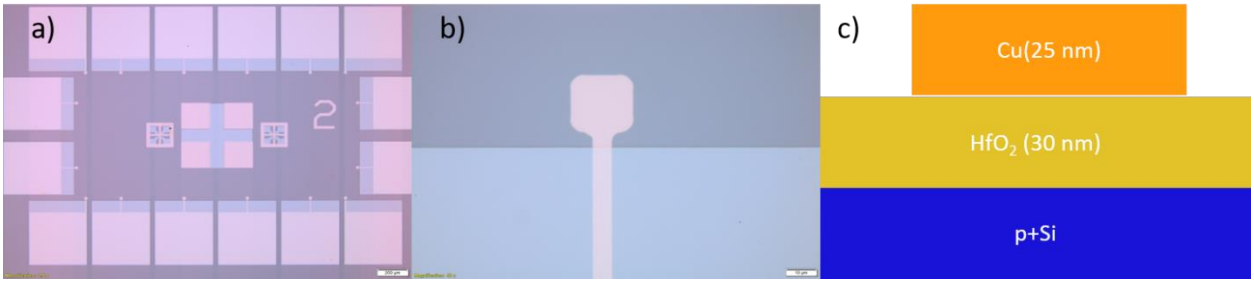

Figure 2: Part a) shows the device layout. This is one of several squares of devices that would appear on one sample. The large outer rectangles are bond pads, while the small rectangles on the inner side are the devices. A close-up image of a device is shown in part b). Part c) shows the thickness of each of the layers of a device.

Forming conditions

Conductive filaments in devices were formed using a Keithley 4200-SCS semiconductor parameter analyzer. The compliance current (the highest current that the instrument will allow to flow through the device) was set at or below 1 mA to limit permanent filament formation caused by an excess of current. In each test, one probe tip was placed in contact with the bottom electrode and the other with the bond pad of the device being formed. The bottom electrode was grounded while a constant positive bias was applied to the bond pad and top contact. Form times had to be long enough to be recordable but short enough that many devices could be formed. Therefore, the range of forming voltages for each sample was based on obtaining a range of forming times from around 10^4 seconds to the smallest consistently recordable time. Current vs. time curves were obtained for all devices, and the times at which device formation began and ended were recorded.

Conductive Atomic Force Microscopy

After device formation, the surface topography of the top electrodes was examined using a Bruker Dimension Icon atomic force microscope (AFM) in tapping mode. Any unusual morphology was noted and imaged. The copper electrodes were then removed by wet etching in 0.5% $FeCl_3$ for 15 seconds. The devices were examined under the Bruker AFM again, this time using c-AFM mode and a conductive platinum-coated tip (MikroMasch HQ: NSC18/Pt, f_o = 75 kHz, k = 2.8 N/m, coated tip radius < 30 nm). Any unusual morphology was examined at higher magnification, as conductivity in scans larger than 20 μm might be represented in only one image pixel. Conductivity was measured at -5.0 mV applied bias between the tip and stage, with a sensitivity range of 1 nA/V. In some cases, the set-point was increased to improve contact between the tip and oxide layer. The specifics for these tests and the scratch-through test are found in Table 2 below.

Table 2: AFM scanning parameters for each test.

	Top Contact Imaging	HfO_2 Imaging	Scratch-Through
Mode	Tapping	Contact (c-AFM)	Contact (c-AFM)
Setpoint Voltage (mV)	250	100 - 150	300 - 700
Scan Size (μm)	25 x 25	(various)	5 x 1.2
Scan Rate (Hz)	0.5	0.5	0.5
Resolution (Points per line)	384	384	384
DC bias (mV)	---	-5	-5

Scratch-through conductive atomic force microscopy

Of the conductive sites located, the one with the least topographical disturbance was selected for the slice-and-view scalpel c-AFM technique. A 2.5 µm x 0.6 µm area around the region was chosen for scratch-through in order to capture the entire filament, in case the underlying structure slanted away from the top conductive region. The HfO_2 layer in this area was scratched away to a depth of about 30 nm, the thickness of the layer. To scribe down into the HfO_2 layer, a diamond c-AFM tip (Bruker DDESP-V2, f_o = 400 kHz, k = 80 N/m, 0.01-0.025 ohm-cm Sb n-doped Si, front side conductive diamond, back side Al) was utilized. A greater set-point voltage was used for these tests, causing the AFM tip to apply a greater force to the sample, slowly removing nanometer-thin layers of HfO_2 and measuring the topography and conductivity of each layer. Additionally, at 1-2 points during the experiment, continuous scanning was interrupted to take a larger 5 µm scan of the area and measure the etch pit depth. Topography and conductivity data was obtained for each pass of the tip over the area. Topography images were processed via three functions in the Gwyddion software: applying a plane fit, aligning rows according to the median, and zeroing the scale.

CHAPTER III

RESULTS AND DISCUSSION

Device formation and surface topography of damage

In order to obtain a meaningful relationship between forming time, forming voltage, and HfO_2 crystallinity, devices were formed at a range of voltages within in each microstructural oxide suite. The range of forming voltages utilized were 4-8 V for more randomly oriented polycrystalline, 8-10 V for less randomly oriented polycrystalline, and 8-14 V for amorphous devices. The data showed that form time decreased exponentially with increasing forming voltage, but the relationship varied with oxide crystallinity. As shown in Figure 3, the forming voltages required for the more randomly oriented polycrystalline devices were much lower than those required for the other crystallinities.

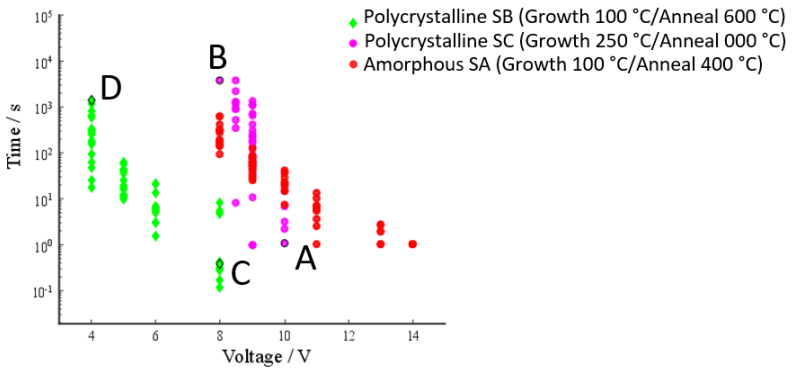

Figure 3: This figure shows the forming time vs. forming voltage for more randomly oriented polycrystalline (SB), less randomly oriented polycrystalline (SC), and amorphous (SA) samples. Devices from sample SB appear to form at the lowest voltages, while SA forms at the highest voltages and SC is in between. A, B, C, and D mark the devices which were imaged with AFM and are shown in Figure 4.

The form time also decreased exponentially with increasing voltage at different rates depending on the oxide crystallinity: the sharpest decrease occurred for the less randomly oriented

polycrystalline sample, while the other two crystallinities showed similar, shallower trends. There is a large amount of variability in the form time when voltage and sample are held constant, but the magnitude of the variability does not appear to depend on the voltage or crystallinity.

A possible explanation for the dependency of forming voltage on oxide crystallinity is the ease of Cu^+ transport through the oxide layer. According to Lanza et al., filaments tend to form along grain boundaries in HfO_2 [12]. While the device structure is not the one used here, the same may be true of our devices, which would explain the lower voltage required to form a filament in the polycrystalline samples, which have grain boundaries, as opposed to the amorphous sample, which does not. However, this would not explain the difference in forming voltage between the two polycrystalline samples.

The topographic AFM images of formed devices with and without the top contact show a range of damage patterns which differ with crystallinity, and an increase in the total damaged area with increasing forming voltage for both crystallinities. 2-3 devices from each voltage level in the data set in Figure 3 were imaged using AFM; the four labeled A, B, C, and D were selected for discussion. A and B were taken at a high and low forming voltage from the less randomly oriented polycrystalline sample, while devices C and D were taken from the more randomly oriented polycrystalline sample. AFM scans of damaged areas were obtained for all devices, first tapping mode AFM with the top Cu contacts on, then c-AFM after removal of the top contacts. Damage was observed for all four devices, typically near the edge of the device, but the size and number of damaged areas varied based on forming voltage and oxide

crystallinity. The morphology of the damage appears roughly the same with the top contact on or off. Figure 4 shows the results of the AFM and c-AFM scans. The damaged areas of devices

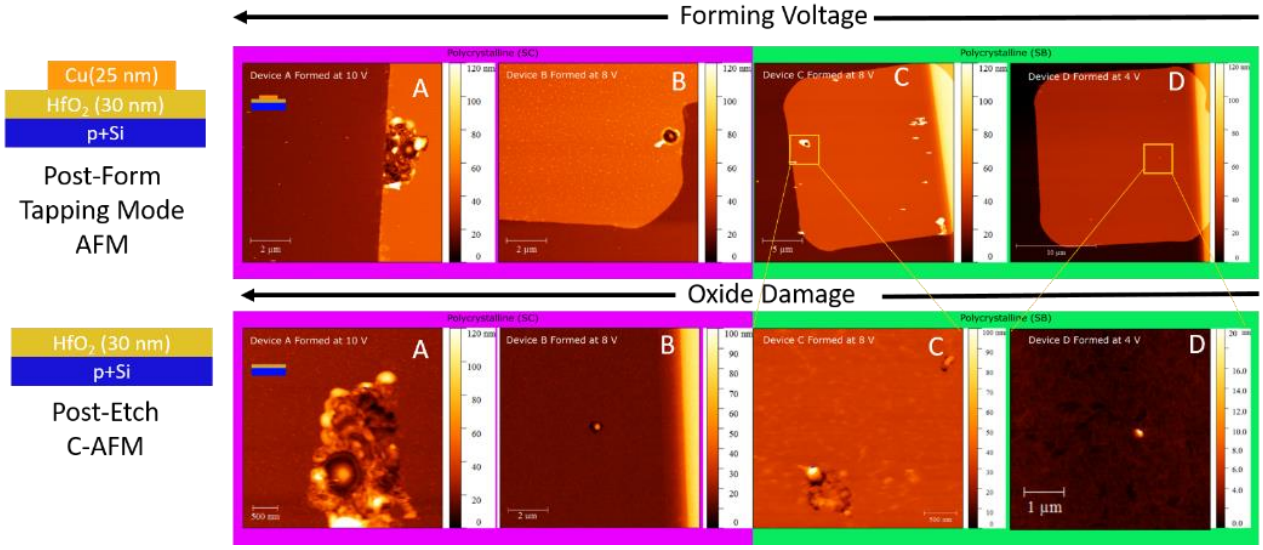

Figure 4: AFM scans for samples SB and SC. The top row shows the topography of the top contact while the bottom row shows the topography of the HfO2 layer after the Cu layer has been removed via wet etch. Devices A and B are from SC, the less oriented polycrystalline sample, while devices C and D are from SB, the more randomly oriented polycrystalline sample. Within a crystallinity group, the devices on the left were formed at a higher voltage than those on the right. For devices with the same crystallinity, oxide damage appears to increase with increasing forming voltage, whether it is an increase in the area of the damage or the number of damaged areas. In addition, devices B and C were formed at the same voltage (8 V). Device C shows greater damage. This implies that damage levels increase with increasing random orientation when forming voltage is held constant.

A, B, and C were all found near the edge of the device, though the damage in device D was between the center and the edge. The damaged areas all had slightly different morphology, but each had a hillock that rose above the surrounding surface. The hillocks all had different heights; compared to the HfO_2 layer, the heights for A, B, C, and D were about 50 nm, 30 nm, 60 nm, and 20 nm. In devices A and B, a small "moat" of materials around 20 nm lower than the HfO_2 surface surrounded the hillock. The moat in device A was further surrounded by damaged areas both higher and lower than the HfO_2 surface, with and without the top contact. The damaged area was around 4 µm x 2 µm. In device B, the moat was surrounded with a ring of higher topography when the top contact was present, but the ring disappeared after the wet etch;

the damaged area was around 700 nm. Device C did not have the moat; the damage area that was examined consisted of the hillock and a slight depression of nearby HfO_2 and had an area of around 750 nm x 700 nm. The damage to device D appeared to be only the hillock, which was about 250 nm in diameter. Device C had the highest number of damaged areas, while device A had the largest damaged area. These two devices were each formed at the higher voltage for their sample. Device damage therefore increases with increasing forming voltage, for devices with the same crystallinity. However, device damage is also dependent on the oxide crystallinity, as can be observed by considering devices B and C. Device C has greater damage than device B despite being formed at the same voltage level.

The damage observed may be an effect of dielectric breakdown. If this is the case, the dependence on forming voltage could be due to power dissipation. When the voltage is greater, the power dissipated through the sample will be greater, resulting in more damage. The presence of more damaged areas, as in device C, could indicate multiple sites where breakdown occurred. It is possible this difference in number of breakdown sites was caused by the difference in crystallinity. This difference in crystallinity could also be related to the difference in damage pattern; devices A and B appear to have a similar pattern with a hillock and moat, while C and D have the hillock but no moat. However, until we understand what caused the damage, it is difficult to determine why specific damage patterns appear.

In addition to the topography data shown in the bottom half of Figure 4, conductivity data was obtained during the same scan. Conductive spots, located within the damaged regions but with a much smaller area, were found for three of the devices (A, C, and D). These conductive spots were typically found near the edge of a high-topography region, not necessarily the hillock. It is possible that their apparent location was influenced by the AFM tip's contact with that area.

The tip would have greater contact with high topography than with low topography, and greater contact leads to a stronger conductive signal. The conductive region could be larger, or there could be more conductive regions, which do not appear on the scan because they are associated with lower topography. The presence of conductive regions is explained by the filament model.

c-AFM etching tomography of conductive filaments

Due to its low level of topographic disruption, the conductive region associated with the hillock on device D was selected for investigation via c-AFM etching, the results of which revealed an hourglass-shaped filament associated with the hillock. The 2D topographic and conductivity data from selected layers of the scratch-through are displayed in Figure 5.

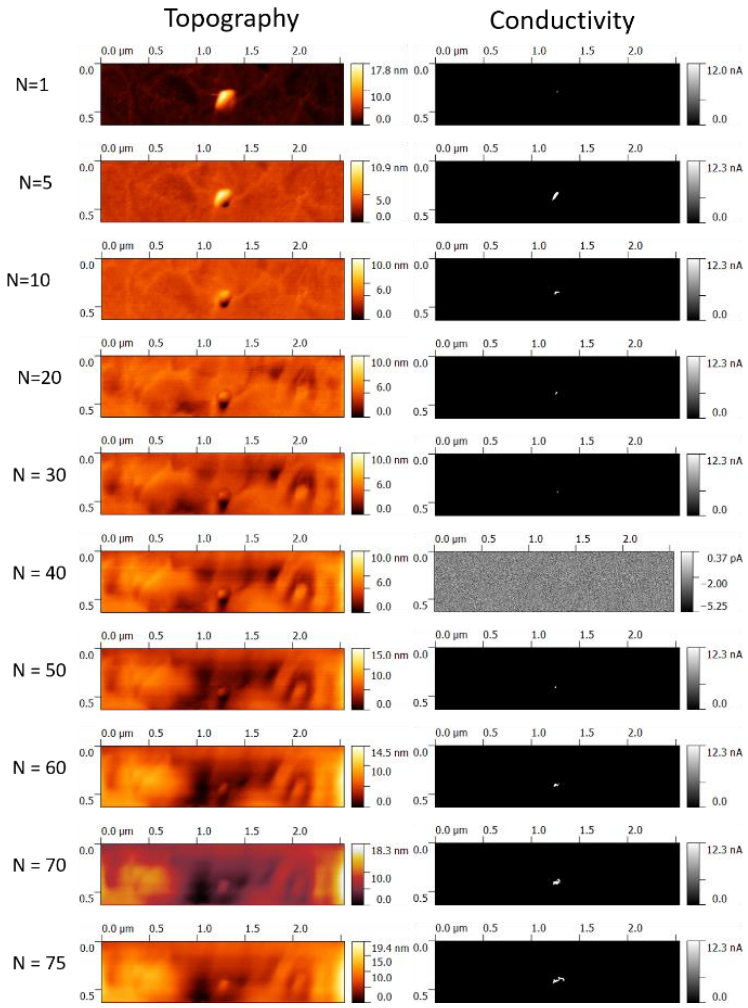

Figure 5: 2D scans of topography and conductivity data are shown for the conductive region of device D. N=1 is the first layer taken, at the top of the HfO2 layer; as N increases, the images move further down towards the p+Si contact.

Topographic data reveals that conductivity is initially associated with the 20-nm protrusion within the oxide layer. Note that conductivity saturates the detection circuit at 12 nA measured at -5.0 mV. The RMS noise floor for this instrument is approximately 2 pA. As the diamond tip etches down below the plane of the oxide layer itself, the protrusion persists, and a well develops adjacent to the hillock. Conductivity is still associated with the hillock and well, but begins to spread deeper within the HfO2 layer. Additionally, the topographic data helps account for drift when determining the shape of the filament. Initially, no conductive signal was detected, but

after a few passes the signal appeared. This suggests the presence of a thin insulating layer on top of the filament, which could be explained by the oxidation of the copper exposed to air. Based on aligned conductivity maps, it appears that the filament was initially around 100 nm in width and narrowed as the AFM tip scratched further into the HfO_2, until it became too thin for the tip to register (< 30 nm). Eventually the filament widened again (up to 100 nm), and as the AFM tip approached the bottom p+Si layer, the filament split into three conductive segments. A schematic of the filament morphology is shown in Figure 6.

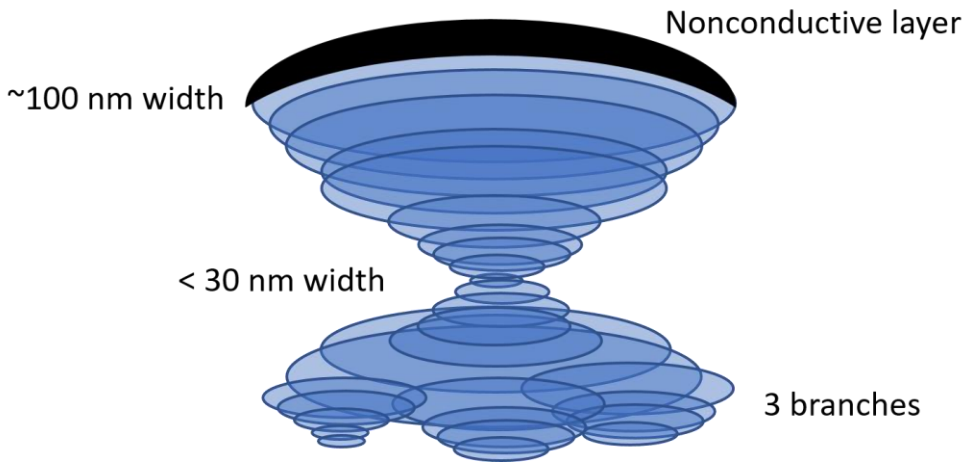

Figure 6: 3D schematic of filament morphology.

The etch rate into the HfO_2 layer was non-linear, slowing as the diamond coating of the tip was gradually worn down. Practically speaking, the first 150 scans were physically spaced much further apart than the last 200.

Figure 7 shows the trench left behind in the HfO_2 layer after the scratch-through experiment was completed. The depth of the trench is approximately 25 nm, which is the thickness of the HfO_2 layer. This demonstrates that we were successful in scratching through the majority of the layer, although we never reached saturation on the entire conductivity map, which would indicate complete removal of the HfO_2 and contact with the p+Si layer.

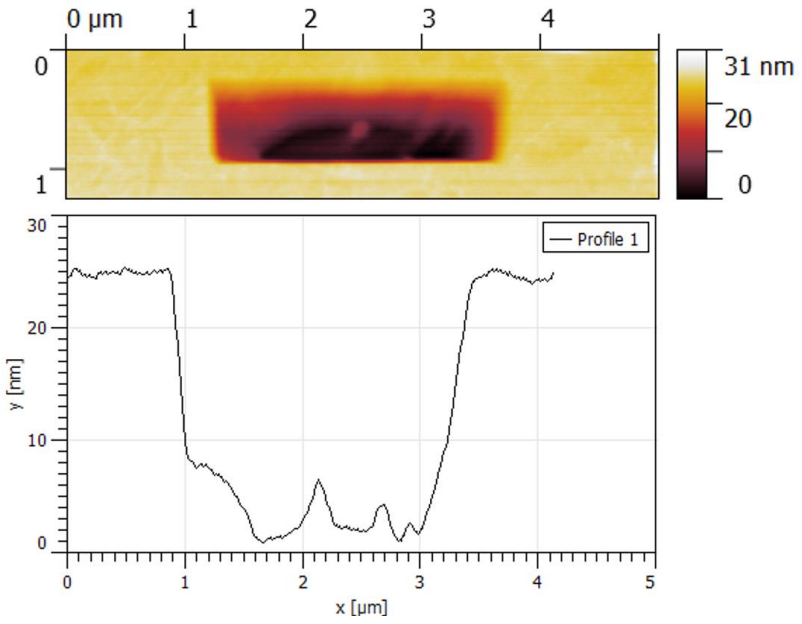

Figure 7: Figure 7a shows a c-AFM image of the trough left after the scratch-through experiment was performed. Figure 7b shows a depth profile of the trough. The depth of the trough is approximately 30 nm, which demonstrates that the entire HfO2 layer was scratched through and imaged.

The scratch-through experiment results confirm the existence of a conductive filament in a formed p+Si|HfO_2|Cu device. The filament appears to have an hourglass shape, unlike the findings of the studies by Celano et al. [13, 15], which reported a conical morphology with the point near the bottom electrode. The devices in this study were TiN|Al_2O_3|Cu, and filaments were thought to be composed of Cu^+ ions; the conical shape was interpreted as evidence that filament formation was Cu^+ transport limited. Our devices have the same top contact and the same predicted filament composition, but the widening of our filament before it reaches the bottom electrode indicates that the Cu^+ ions reaching the bottom contact is not the limiting factor in filament formation. The difference in limiting factors could be due to the different oxide layers; Cu^+ ions may migrate more easily in HfO_2 than in Al_2O_3. Another paper by Mehonic et al. discusses the narrowing of a resistive switching filament to a quantum point contact before it is reset [16]. Our filament could very well approach this point when it thins to the point that it is

no longer detectable by the AFM. Its shape would then imply that the last part of the filament to be formed is the thin middle section where the quantum point contact would be made. Further studies on cycled devices would help confirm or reject this possibility.

CHAPTER IV

CONCLUSION

In conclusion, p+Si|HfO_2|Cu devices were formed at constant bias and examined under AFM and c-AFM to investigate device damage and potential filament sites. One conductive site was examined using scratch-through c-AFM to obtain a 3D tomogram of a conductive filament. While surface c-AFM scans have been performed before on HfO_2 devices [9, 10, 12], a scratch-through experiment with HfO_2 has not been reported. First, we observed that more randomly oriented polycrystalline devices formed at much lower voltages (4-8 V) than amorphous devices (8-14 V). This is likely because filaments typically form along grain boundaries [12], which were not present in the amorphous sample. We also saw a decrease in form time with increasing forming voltage for all samples. This was unsurprising; as we apply a greater driving force, ion migration happens more quickly. From the AFM and c-AFM scans of formed devices, we found that all the damaged areas contained a hillock that ranged from 20 to 60 nm in height. However, the rest of the damage displayed different patterns, which appeared to vary with oxide crystallinity, and different damage areas, which depended on both forming voltage and crystallinity. The dependency on forming voltage is likely due to a higher power dissipation, while the dependency on crystallinity is not clear. c-AFM scans showed that a conductive region is typically associated with a hillock on the surface of the HfO_2 layer, though it is much smaller than the hillock itself. One of these conductive regions was examined using scratch-through c-AFM, which was used to construct a schematic of the 3D morphology of the filament. The filament appears to possess an hourglass shape, which differs from the conical shape reported for TiN|Al2O3|Cu devices in studies by Celano et al. [13, 15]. The hourglass shape implies that,

unlike the devices in the Celano study, ion transport to the bottom electrode is not the limiting factor in filament formation.

The next step in this line of research is to examine more filaments and determine if they have similar morphology to the one observed here. However, in order to learn more about how filaments form in an actual device and how they might contribute to device variability, studies must be performed on devices that have been cycled. Scratch-through studies on filaments in devices in the low resistance state will be similar to the one conducted here, but those in the high resistance state will be different, since the filament will be partially or wholly disrupted. The area of the filament will have to be estimated based on the damage to the oxide layer, and several layers of HfO_2 will have to be scratched away before the bottom half of the hourglass of the conductive filament is reached, if it is in fact still present. Depending on ion transport during filament rupture and setting, the filament may look entirely different in different states; these differences will be observed and investigated. In addition, we will look into how the filament shape changes with a decrease in the thickness of the HfO_2 layer. It is unknown whether the filament shape will scale with the thickness, or whether a portion of the hourglass would be removed (potentially forming a cone). Investigating these possibilities will yield more information about filament morphology and allow greater insight into the mechanisms of filament formation and rupture.

REFERENCES

1. Kwon, D.-H., et al., *Atomic structure of conducting nanofilaments in TiO2 resistive switching memory.* Nature nanotechnology, 2010. **5**(2): p. 148-153.

2. Choi, S.J., et al., *In Situ Observation of Voltage-Induced Multilevel Resistive Switching in Solid Electrolyte Memory.* Advanced Materials, 2011. **23**(29): p. 3272-3277.

3. Kwon, J., et al., *Transient Thermometry and High-Resolution Transmission Electron Microscopy Analysis of Filamentary Resistive Switches.* ACS Applied Materials & Interfaces, 2016. **8**(31): p. 20176-20184.

4. Liu, Q., et al., *Real-Time Observation on Dynamic Growth/Dissolution of Conductive Filaments in Oxide-Electrolyte-Based ReRAM.* Advanced Materials, 2012. **24**(14): p. 1844-1849.

5. Strachan, J.P., et al., *Direct identification of the conducting channels in a functioning memristive device.* Advanced Materials, 2010. **22**(32): p. 3573-3577.

6. Xu, Z., et al., *Real-time in situ HRTEM-resolved resistance switching of Ag2S nanoscale ionic conductor.* ACS nano, 2010. **4**(5): p. 2515-2522.

7. Yang, Y., et al., *Electrochemical dynamics of nanoscale metallic inclusions in dielectrics.* Nature communications, 2014. **5**.

8. Calka, P., et al., *Chemical and structural properties of conducting nanofilaments in TiN/HfO2-based resistive switching structures.* Nanotechnology, 2013. **24**(8): p. 085706.

9. Brivio, S., et al., *Formation and disruption of conductive filaments in a HfO2/TiN structure.* Nanotechnology, 2014. **25**(38): p. 385705.

10. Deleruyelle, D., et al., *Direct observation at nanoscale of resistance switching in NiO layers by conductive-atomic force microscopy.* Applied physics express, 2011. **4**(5): p. 051101.

11. Iglesias, V., et al., *Dielectric breakdown in polycrystalline hafnium oxide gate dielectrics investigated by conductive atomic force microscopy.* Journal of Vacuum Science & Technology B, Nanotechnology and Microelectronics: Materials, Processing, Measurement, and Phenomena, 2011. **29**(1): p. 01AB02.

12. Lanza, M., et al., *Grain boundaries as preferential sites for resistive switching in the HfO2 resistive random access memory structures.* Applied Physics Letters, 2012. **100**(12): p. 123508.

13. Umberto Celano, L.G., Attilio Belmonte, Karl Opsomer, *Three-Dimensional Observation of the Conductive Filament in Nanoscaled Resistive Memory Devices.* Nano Letters, 2014(14): p. 2401-2406.

14. Umberto Celano, L.G., Attilio Belmonte, Karl Opsomer, *Understanding the Dual Nature of the Filament Dissolution in Conductive Bridging Devices.* The Journal of Physical Chemistry Letters, 2015(6): p. 1919-1924.

15. U. Celano, G.G., L. Goux, A. Belmonte, M. Jurczak, W. Vandervorst, *Nanoscopic Structural Rearrangements of the Cu-Filament in Conductive-Bridge Memories.* Nanoscale, 2016.

16. Mehonic, A., et al., *Structural changes and conductance thresholds in metal-free intrinsic SiOx resistive random access memory.* Journal of Applied Physics, 2015. **117**(12): p. 124505.